Design and Development of a Wheel-less Snake Robot with Active Stiffness Control for Adaptive Pedal Wave Locomotion

Mohammadali Javaheri Koopaee[*1], Sander Bal[1], Christopher Pretty[1], XiaoQi Chen[2]

1. Mechanical Engineering Department, University of Canterbury, Christchurch 8041, New Zealand.
2. Manufacturing Futures Research Institute, Swinburne University of Technology, Hawthorn 3122, Australia.

Abstract

This paper presents the design and manufacture process of a wheel-less, modular snake robot with Series Elastic Actuators to reliably measure motor torque signal and investigate the effectiveness of active stiffness control for achieving adaptive snake-like locomotion. A Polyurethane based elastic element to be attached between the motor and the links at each joint has been designed and manufactured using water jet cutter, which made the final design easier to develop and more cost-effective, compared to existing snake robots with torque measurement capabilities. The reliability of such torque measurement mechanism examined using simulated dynamical model of pedal wave motion, which proved the efficacy of the design. A distributed control system is also designed, which with the help of an admittance controller, enables active control of the joint stiffness to achieve adaptive snake robot pedal wave locomotion to climb over obstacles, which unlike existing methods does not require prior information about the location of the obstacle. The effectiveness of the proposed controller in comparison to open-loop control strategy has been shown by the number of experiments, which showed the capability of the robot to successfully climb over obstacles with the height of more than 55% of the diameter of the snake robot modules.

Keywords: Modular snake robot; series elastic actuator; active stiffness control; pedal wave locomotion; adaptive locomotion

1 Introduction

Snake robots are of interest in the field of bio-inspired design, particularly in regards to locomotion. The small cross section of these robots, like their natural counterpart makes them ideal for locomotion in narrow and unstructured environments[1]. Moreover, snake robot locomotion mechanism is inherently stable, compared to other means of locomotion like walking, which makes it suitable for inspection[2], exploration of remote or hazardous environments[3], and locomotion on uneven terrains[4].

Historically, the general belief among zoologists was that snakes use their scales or tips of their ribs in a similar manner that other animals use their legs as means of locomotion[1]. In 1879, Hutchinson[5]

[*]**Corresponding Author:** Mohammadali Javaheri Koopaee
Email: mohammadali.javaherikoopaee@pg.canterbury.ac.nz

challenged this theory and provided his successors, such as Mosauer[6] and Gray[7] with the insight to explain the snake locomotion mechanisms, which led to identification of four major types of snake locomotion, namely lateral undulation, sidewinding, concertina and rectilinear motion. The aforementioned critical findings, enabled Hirose to further analyze bio-snakes movement and fabricate the world's first snake robot in 1972[1], which could perform 2D lateral undulation, with the use of passive sideways wheels to mimic the effect of anisotropic friction of real snakes.

Unlike the snake robot developed by Hirose and more recently by others[4], it is has been shown that biological snakes movement is not purely planar[8] and robot designs based on this discovery, have proven to be very effective for real world applications[2]. However, these types of snake robots, which are not equipped with passive wheels and do not have anisotropic friction property of belly scales of their natural counterpart (see Hopkins *et al*.[9] and the references therein for more information about common snake robot designs.) belong to the under-actuated robotic systems family, for which real-time control methods are difficult to implement. Consequently, most of the locomotion control strategies for snake robots are based on generating biologically inspired periodic joint angles commands (gait patterns) to achieve a desired type of motion.

Although, these pre-specified snake-like gait patterns are very effective for locomotion on smooth surfaces, they are not suitable for unstructured environments, where direction and magnitude of reaction forces from the environment are difficult to predict[10]. To address this issue, some works, have considered gait parameter adaptation based on body friction[11] and tilt angle feedback[12]. However, these works have only considered locomotion on relatively smooth surfaces and not uneven terrain. Others have proposed a shape based control scheme for pedal wave locomotion of snakes[13] that requires prior information about the environment. More recent works have proposed a control mechanism based on torque control for a snake-like robot[14]. However the controller also requires information form a pressure sensor attached to the surface of the links.

On the other hand, compliant locomotion on uneven terrain, which has been demonstrated to be very effective for walking robots[15], has not yet been fully investigated for snake-like locomotion in

unstructured environment. Vespignani *et al*. have added a passive compliant element in series between the robot joints[16] and Kandhari *et al*. have developed a soft bodied worm-like robot with passive compliance[17], however, in both of these studies experimentation in unstructured environment is not conducted and, because of using a passive flexible element without a motor torque measurement mechanism, the stiffness of the joint could not be varied during the locomotion. Although Whitman *et al*. have mentioned joint admittance control[18], compliance at joint level has not been achieved and the measured external torque is treated as a feedback signal from the environment to modulate the gait parameters for obstacle-aided locomotion, similar to a CPG (Central Pattern Generator) based controller with environmental feedback. Similar works has also been reported by designing a snake robot with compliancy at joint level[19], however no active stiffness control strategy is presented and the developed wheeled snake robot has only been tested on a smooth surface with variable friction and/or inclination.

To fully investigate the effect of active stiffness control implemented on a physical snake robot for locomotion on uneven terrain, designing a custom built force/torque sensing mechanism for robot joints is necessary. Considering the space limitation when dealing with snake robots, this task is even more challenging. Prior works with FSRs (force sensor resistors) [20], strain gauges[21] and a complex, custom made torque sensing system based on a cam mechanism[22], have tried to equip the snake robots with sensitive torque/force mechanisms. However, such mechanism are either complex or very vulnerable to impact as they are attached to the surface of the links. More recently, design of a snake robot equipped with Series Elastic Actuators (SEA), which are capable of torque measurement is presented[23]. However, manufacturing of such an actuator still requires compression moldings and a relatively complicated process for bonding the rubber to a metallic material for manufacturing the elastic part. On the other hand, design of a polyurethane-based compliant element for turning conventional servos into SEAs has proved to be very effective for robotic arms[24]. Employing this idea, which reduces the final cost of the prototype considerably, it is now possible to manufacture an inexpensive snake-like robotic mechanism with SEAs to investigate the effect of compliancy in snake locomotion.

To overcome these limitations, this paper presents the design and testing of an inexpensive wheel-less snake robot with a torque sensing mechanism achieved using a polyurethane based elastic element between the links and the motors. Employing this idea, it is possible to manufacture an elastic element with desired shape and stiffness using easily an accessible polyurethane sheet and attach it between the links and the motors to equip existing snake robots with torque sensing mechanism. Thus, this torque measurement mechanism, unlike others, which requires redesigning every modules of the robot[22] can easily be implemented on existing designs. Moreover, unlike existing methods[20,21], in which the sensing device should be attached to the surface of the links, the polyurethane-based compliant element is embedded inside each joint, thus the final prototype is more robust in design. Additionally, employing the torque measurement mechanism the idea of active stiffness control for snake robots is proposed and implemented using a distributed admittance controller to achieve adaptive autonomous pedal wave locomotion for the first time, which unlike existing methods[13], which the position and height of the obstacle should be known no prior knowledge about the location of the obstacle is required. The applicability of the proposed design and control strategy is illustrated by number of experiments, which shows high adaptability of the snake robot, when autonomously crawling over an obstacle with the height of more than 55% of the diameter of snake robot modules.

The rest of this paper is organized as follows. In Section 2, design and manufacture of the SEA and 3D printed robot joints are presented. In Section 3, pedal wave locomotion on smooth surfaces with proposed design is discussed and experimental and simulation results are compared. In Section 4, an admittance controller for robot joints is implemented and the stability condition is obtained. Moreover, the idea of stiffness control is introduced and its effectiveness is illustrated when the robot is moving over a stair-type obstacle.

2 Development of the snake robot

In snake robots, the size, final cost, overall shape and weight of the robot limits our choices for actuators and sensors. These constraint the designers to use highly geared servo systems to achieve high

output torque at low speed using a small actuator. However, highly geared servo systems with stiff joints, suffer from number of disadvantages, such as backlash, friction and gear break down[25]. These nonlinear effects, make torque estimation based on current feedback ineffective.

One way to design a snake robot with sensitive torque measurement mechanism necessary for compliance control is by attaching an elastic element of known stiffness between the load and motor shaft. Employing these Series Elastic Actuators (SEAs)[25] it is possible to measure the torque based on the deflection of an elastic material. Moreover, the sudden large, external forces on the output shaft, the main reason for gear damage, will be minimized, making the interaction between the robot and environment considerably safer. Energy storage is another advantage of these actuators, which makes them more efficient. Hence, it is worthwhile to make the actuator "softer" and consequently sacrifice the position control loop bandwidth in order to achieve some desirable properties, such as compliance[26].

2.1 Design and manufacture of SEA

To design a Polyurethane-based elastic element to be placed between the servo motor and the each robot link, it is necessary to first determine the material and required characteristics of such element, such as the size and stiffness. For the snake robot design, the main consideration is to make the joints of the robot as light as possible and use the elastic element for measuring a maximum torque of 0.8 Nm with resolution of 0.05 Nm using a 12-bit encoder. For the elastic material, Polyurethane sheet with a thickness of 4 mm and Shore Hardness of 95A proved to be suitable and is easily obtained, hence it was chosen as the material of the design. To decide on the shape of the element, motivated by the work done by Martins *et al.*[24], an initial design with "S" shape blades connecting two concentric rings as shown in Fig. 1.a were chosen to be modified based on simulation results to achieve desired specifications.

The tests conducted by applying 0.05Nm torque to the outer ring while holding the inner ring fixed, which revealed that the compliance predominantly depends on the shape and thickness of the "S" shape blades. Considering the initial design specifications, these two factors have modified and as a result the

optimum width of the blades was found to be 2.5 mm with the blades shape shown in Fig. 1a. The results of the Finite Element Analysis (FEA) of the final prototype is shown in Fig. 1b., where the maximum displacement is shown in red.

It should be noted that although Martins *et al.*[24] have claimed that the final part can be manufactured with a CNC router without using any refrigeration fluid, we found this method to be impractical. Hence, once the design was optimised in the simulation, water jet cutter was used to manufacture the final elastic part as shown in Fig. 1c, which is a relatively simpler and more cost effective manufacturing process, compared to compression molding used by Rollinson *et al.*[23].

2.2 Modelling and calibration of SEA

For calibration of the manufactured part, a 12-bit digital magnetic rotary encoder used to measure the relative angular displacement between the inner and outer rings. A specific sensor holder was designed and manufactured so that the magnet was attached to the inner ring and the sensor board to the other ring, thus enabling direct measurement of relative angular displacement between the inner and other rings with the use of a single rotary encoder.

To calibrate the elastic element, a test rig was manufactured using a 3D printer, which allowed known weights to be attached to the outer ring while the relative angular displacement was measured. To calibrate the elastic element, the servo system was fixed at a complete horizontal position and elastic element modelled as a torsional spring. The static equation then obtained to be as follows:

$$\tau_e + \tau_{arm} = \mathrm{K}(\theta - q) \tag{1}$$

where τ_e is the external moment acting on the link due to the weights attached to it, τ_{arm} is the moment due to the weight of the link, K is stiffness coefficient of the spring to be obtained, $\theta = 0$ is the motor angle and q is the joint angle. Considering that weights will be attached to the link with the elastic element is in normal shape, the distance between the point of the action of the external force to the center of rotation is known and motor is fixed at a certain angle, (1) can be simplified to:

$$\tau_e = mgdcos(q) = -\mathrm{K}q, \tag{2}$$

where m is the mass of the attached weight and d the distance between the point of the action of the external force and the centre of rotation.

Using equation (2) the elastic element calibrated and the results of calibration are shown in the Fig. 2. The resolution of the sensor then calculated to be 0.01 Nm, exceeding the design requirements. Based on these results and considering a simple zero order system, the SEA modelled as a torsional spring with no damping, and spring constant K = 1.74 Nm/rad.

2.3 Design and manufacture of the robot modules

In this section, design and manufacture of the snake robot modules, equipped with the SEA will be discussed. It should be noted that unlike other works[19], the designed snake robot modules, shown in Fig. 3 are not equipped with wheels, hence this robot is more suitable for locomotion in challenging environment, such as unstructured confined spaces and cluttered environments[27], where wheeled snake robots suffer from the same limitations of wheeled robots.

As shown in Fig. 3, each module of the proposed design of the robot consists of two main parts. The Body part as shown in Fig. 3.a, is designed to accommodate the actuator (Herkulex smart servo, DSR-0101) with the specifications shown in Table 1, a custom made control board and the elastic element without interfering with the joint motion. The connector part in Fig. 3.b, connects each module to the following module, where hollow spaces are considered for easy wiring. Moreover, a sensor holder as shown in Fig. 4 is also designed to be mounted between the elastic element and the connector part, which accommodates the magnetic encoder (Ams, AS5145) and make sure that the attached magnet to the elastic part is fully aligned with the sensor. The final CAD model of a single module is shown in Fig. 4.

It should be mentioned that, screw holes on the connector and the body part are designed such that each joint can be connected to previous joint with 90 or zero degrees relative rotation about longitudal axis. This together with the symmetrical octagon shape of the links allows the same design to be used, without major changes for pedal wave motion, lateral undulation or 3D motion generation. Finally, an electronic system has also been designed to equip each joint of the robot with a custom made circuit

board for power distribution, communication, data acquisition and control of the joint. The final robot module, manufactured with a cost-effective 3D printer using Acrylonitrile Butadiene Styrene (ABS) as the main material is shown in Fig. 5, where the elastic element is embedded inside of each joint, which makes the torque measurement mechanisms more robust compared to existing designs with strain gauges attached to the surface of the links[21].

It should be noted that, using the custom made control board, each module can directly receive gait pattern parameters as a command from the external main controller, with the use of the communication system designed based on CAN bus. Moreover, each module can also request data form other joints on the bus, which makes the design very suitable for implementation of CPG based motion generation, where direct feedback from neighbouring joints is necessary.

3 Pedal wave locomotion on smooth surfaces

As mentioned earlier, snake robot motion control is usually based on generating the desired joint angles as a repetitive sequence of commands by means of a parametric nonlinear oscillator and employing a PID controller at joint level to track the desired angles. For planar snake motions, such as lateral undulation or pedal wave motion, the gait pattern is usually chosen to be a parametric sinusoidal wave as follows[28]:

$$q_j = A\,sin\big(\omega t + \phi(j-1)\big) \tag{3}$$

where $q_j;\ i = 1,2,\dots,N$ are joint angles, ω is the temporal frequency, ϕ is spatial frequency and A is amplitude of the sinusoidal wave. It should be noted that gait equation (3) can easily be extended to 3D case by considering a second sinusoidal wave for perpendicular joints.

To show the effectiveness of the proposed design, the developed snake robot has been assembled with five planar joints to perform pedal wave motion[13] (also known as travelling wave locomotion[29], caterpillar-like motion[30] or inchworm motion[31]). To achieve this type of motion, the sinusoidal motor angles are generated based on gait equation (3) with $A = \frac{\pi}{6} rad$, $w = \pi\, {rad}/{sec}$ and $\phi = \frac{-2\pi}{5}\ rad$, where Fig. 6 shows the snake robot performing this type of motion and moving forward with average

speed of 4.5cm/sec. This shows that although a flexible element is attached between the motor and joints, the robot still can achieve the desired motion on smooth surfaces.

To show the effectiveness of the proposed torque measurement mechanism, it is critical to compare the simulation and experimental results. To simulate the pedal wave locomotion of the snake robot one can use the dynamical model presented by Akbarzadeh *et al.*[32] based on Euler Lagrange method and employ a spring damper contact model to compare the required motor torque to perform pedal wave motion with the experimental results provided by the torque sensing mechanism.

To obtain the equations of motion of the robot, one should consider the body shape of a 2D snake robot as shown in Fig. 7, where $\theta_i, i = 1,2, \dots, N$ is the absolute link angle of i^{th}link, $q_j, j = 1,2, \dots, N-1$ is the relative angle between the links, $[x_i, z_i]$ is the position of center of mass of i^{th}link in the global coordinate frame, $2l$ is the length of each identical link and $[p_x, p_z]$ is the centre of mass of the robot.

Considering the expression for the kinetic energy of the system due to the translational and rotational velocity of the links and the potential energy of the system due to gravity (see Akbarzadeh *et al.*[32]), it is now possible to construct the equations of motion of pedal wave motion as follows:

$$\boldsymbol{M}(\boldsymbol{q})\ddot{\boldsymbol{q}} + \boldsymbol{C}(\boldsymbol{q}, \dot{\boldsymbol{q}}) + \boldsymbol{G}(\boldsymbol{q}) = \boldsymbol{Q}^{\tau} + \boldsymbol{Q}_1^f + \boldsymbol{Q}_2^f \tag{4}$$

where $\boldsymbol{q} = \left[q_1, q_2, \dots, q_{n-1}, \theta_N, p_x, p_y \right]^{\mathrm{T}}$ is the generalized coordinate, $\boldsymbol{M}(\boldsymbol{q})_{(N+2)\times(N+2)}$ is the positive definite links inertia matrix, $\boldsymbol{C}(\boldsymbol{q}, \dot{\boldsymbol{q}})_{(N+2)}$is the vector of Coriolis and centrifugal terms, $\boldsymbol{G}(\boldsymbol{q})$ is a column vector of gravitational forces, $\boldsymbol{Q}^{\tau}$ is the vector of N-1 control inputs, $\boldsymbol{Q}_1^f$is the vector of friction forces (depending on the friction model) and $\boldsymbol{Q}_2^f$ is the vector of other external forces due to contact with the environment. (See Appendix. A and B for the details about the structure of the model.)

It should be noted that, although obtaining the expression for the kinetic and potential energy of the system is straight forward, calculation of the vector of non-conservative external forces $\boldsymbol{Q}_2^f$, requires modelling the interaction between the environments and the robot. Hence, in pedal wave motion, which modelling the contact between the robot links and the ground is required, one can use the well-known

spring damper contact model as shown in Fig. 8, where f_c^n and f_c^t are the normal and tangential forces exerted at point p_c from the environment

Assuming that p_c is in contact with the ground, i.e. $z^{p_c} \leq 0$, and considering the spring-damper contact model, $f_c^n$and f_c^t can be calculated as follows:

$$f_c^n = Max(k(z^{p_c}) - d\dot{z}^{p_c}, 0) \tag{5}$$

$$f_c^t = -f_c^n \mu sign(\dot{x}^{p_c}) \tag{6}$$

where x^{p_c} and z^{p_c} are the coordinate of the point of contact p_c , μ is the friction coefficient, k is the spring and d is the damping constant of the environment. It should be noted that, in pedal wave locomotion on smooth surface, the normal and tangential vectors n and t align with the Z and X coordinate of the global coordinate frame, hence the contact forces are already expressed in the global coordinate frame.

Finally to obtain $\boldsymbol{Q}_2^f$, it is enough to construct the Jacobian matrix and transform the external forces to joint variable space as follows:

$$\boldsymbol{Q}_2^f = \sum_{c=1}^{P} \begin{bmatrix} \frac{\partial \dot{x}^{p_c}}{\partial \dot{\boldsymbol{q}}} & \frac{\partial \dot{z}^{p_c}}{\partial \dot{\boldsymbol{q}}} \end{bmatrix}^{\boldsymbol{T}} \begin{bmatrix} f_c^t \\ f_c^n \end{bmatrix}, \tag{7}$$

where P is the number of contact points.

Considering this modelling framework, it is now possible to compare the simulation and experimental results. For this purpose a snake robot with six identical links each with the mass of 0.15kg length 0.07m and five motors (same as the designed robot) has been simulated considering the spring and damping constant for modelling the environment to be 25 and 350 respectively. The joint angle commands were generated according to gait equation (3), similar to the conducted experiment to compare the simulation results with the experimental motor torque data obtained from the test. Fig. 9 shows the simulated pedal wave motion of the snake robot, where the joint positions, tip of the head and tail modules and the center of mass of each link are specified with circles (See Online Resource. 1 showing the simulated motion together with the achieved pedal wave motion with the snake robot).

Considering that in a flexible joint, the motor output torque can be estimated as $\tau_M \cong \mathrm{K}(\theta - q)$ [33], the motor torque for two joints, namely the head (First joint) and middle body (Third joint) has been recorded together, as shown in Fig. 10 and Fig. 11.

As can be seen from the Fig. 10 and Fig. 11, estimated motor torque resembles the motor torque signal obtained from the simulation with some expected discrepancy because of the assumed linear model of the elastic element and the uncertainty of the simulation model. Moreover, although for modelling the pedal wave motion of the robot both Coulomb and Viscous friction models have been used, still the model cannot precisely take into account the effect of slipping between the snake and the floor. Hence, slipping, which adversely affect the efficiency of the locomotion pattern in real world environment can be considered as another reason why the measured torque does not exactly match with the simulation results. It should also be mentioned that the middle body joint, which is closer to the center of mass of the robot, located in the middle of the snake body should generate more output torque relative to the head joints, which is far from the center of mass of the robot. This result is a very important design consideration also mentioned by Chen *et al.*[34] as the result of simulation studies.

4 Stiffness control for locomotion on uneven terrain

Taking advantage of the proposed design of the snake robot with torque sensing mechanism, it is possible to actively control the joint stiffness of the robot. In this section, we firstly discuss the main motivation behind stiffness control in snake robot and why we think this strategy could be useful for achieving adaptive locomotion. Moreover, we introduce a disturbed admittance controller and experimentally investigate the effectiveness of such control scheme to achieve adaptive pedal wave motion.

4.1 Motivation

Fig. 12 illustrates the body shape of a 2D snake robot with five joints, performing pedal wave motion at a particular instance in time, where *X*, *Z* define a global coordinate frame, q_i's are the relative joint angles, l_i is the i^{th} body link, $l_{2,6}$ are assumed to be in contact with the ground at points $p_1$and p_2.

In contrast to lateral undulation, in which the robot body is always in contact with the ground, during pedal wave motion and sidewinding (3D generalization of pedal wave motion), the robot lifts some part of its body off the ground and pushes against the ground to move forward. This locomotion mechanism have some similarities with legged locomotion, in which the foot comes into contact with the ground and normal reaction and friction force are the main propulsive force, moving the robot forward.

On uneven surfaces the robot might stick, when the environmental forces in *X* direction cancel each other or rollover to one side when the projection of canter of mass along the gravity force leaves the convex hull of contact points. One way to address this issue is to actively control the dynamics of contact between the robot and environment by utilizing joint level admittance or impedance controllers.

Recently, it has been shown that human runners, actually control their leg stiffness in response to varying terrain for disturbance rejection[35], passive stability[36] and higher efficiency[37]. The analogy between human walking and pedal wave motion of snake robots, suggests that stiffness control strategy could be utilized for more adaptive snake locomotion on uneven terrain.

4.2 Joint admittance control

To design a stiffness controller for the snake robot to achieve adaptive locomotion, we propose a Collocated Admittance Controller (CAC)[38] at joint level, i.e. the position control loop is closed at motor angle level, with the block diagram shown in Fig. 13, where K_d is the desired stiffness, C_p is a PD position controller, M is the single joint model, K is the stiffness of the elastic element, θ is motor angle, θ_r is the desired motor angle generated by gait equation (3), $\theta_s = \frac{\mathrm{K}-K_d}{K_d}\,\tau_e$, q is the joint (link) angle and τ_e is the exerted torque on the environment.

In order to make sure that the resulting closed loop system is stable, it is enough to check the passivity of the impedance relation, $Z(s) = \frac{-\tau_e}{\dot{q}}$, which considering the block diagram in Fig. 13, with $\theta_r = 0$ and joint model $M = \frac{1}{Js^2}$ can be obtained with little effort to be:

$$Z(S) = \frac{\mathrm{K}K_d(JS^2 + C_p)}{S[K_d(JS^2 + C_p) - (\mathrm{K} - K_d) - \mathrm{K}K_d]} \quad (8)$$

It should be noted that to obtain the above relation, it is enough to obtain the transfer function between external torque τ_e and joint angle q employing conventional simplification methods of block diagrams and finally replace q by sq (see Calanca *et al.*[38] for more details).

The passivity condition for $Z(s)$ is equivalent to have (i) $Z(s)$ to be stable and (ii) $Re\ [Z(jw)] \geq 0$. This gives the well-known stability condition of admittance controllers, which the desired stiffness cannot be chosen to be higher than the stiffness of the attached elastic element (i.e. K_d <K)[38], hence for the snake robot joint admittance controller, K_d should be smaller than 1.75.

In the next section, first, this controller will be implemented on a single joint of the robot to study the effect of the proposed joint stiffness controller and finally, the effect of such control strategy on the overall motion of the robot will be investigated in details.

4.3 Results and discussion

To better show how the proposed controller works in practice, first, this controller has been implemented on a single joint of the robot, where θ_r is chosen to be a sinusoidal signal according to equation (3), with $A = \frac{\pi}{4} rad$ and $w = \pi$ (See Online Resource. 2 showing the case with $A = 0$). As shown in Fig. 14.a the joint will be at rest on the ground when $q = 0$, is free to move when $q > 0$ and will push against the ground (i.e. reaction force f_e and torque τ_e will be exerted on the link) when $q < 0$.

During the test, the values of K_d changed, after five complete cycles while the joint was in motion to collect enough samples to investigate the effect of varying joint stiffness on q. The measured joint angle q then recorded while sampled at 10KHz as shown in Fig. 14.b.

As can been seen from Fig. 14.b, the servo motor start to oscillate with $K_d = \mathrm{K}$ while successfully tracking the commanded motor angle even when it touches the ground. This means that at the beginning of the experiment, which $K_d = \mathrm{K}$, the robot push against the ground and no matter how much is the reaction force, the servo motor is only in position control mode and $\theta_r = q$. On the other hand, when

the value of K_d changes to 0.5K, the joint still tracks the commanded trajectory when there is no environmental torque τ_e, however when $q < 0$, the joint pushes against the ground and because $\tau_e \neq 0$ the admittance control comes into effect and depending on the value of K_d the actual joint angle deviates from the commanded trajectory, thus $\theta_r \neq q$. Consequently, this experiment shows that by changing the joint stiffness, the joint angle q can adaptively change during the motion of the robot based on the contact forces from the environment even when θ_r (i.e. gait parameters) remain constant.

Another experiment is also designed to examine the effect of joint level compliance on the overall motion of the robot. In the test, the robot was commanded to start moving based on pedal wave motion pattern (3) with $A = \frac{\pi}{4} rad$, $w = \pi\, {rad}/{sec}$ and $\phi = \frac{-2\pi}{5} rad$ and move over an obstacle with height 36mm and width 107mm located on the robot path as shown in Fig. 15. The experiment conducted on the robot starting from a same initial position relative to the obstacle and repeated five times for $K_d = \mathrm{k}, \frac{\mathrm{k}}{2}, \frac{\mathrm{k}}{3}, \frac{\mathrm{k}}{4}, \ldots, \frac{\mathrm{k}}{10}$, (K is the stiffness of the elastic element) to investigate the effect of joint stiffness.

As a result of the test, the stiff joint strategy with K_d =K (without stiffness control) proved to be totally ineffective in every trial, due to the robot getting stuck or the whole robot "rolling-over" to one side as shown in Online Resource. 3. On the other hand, compliant strategy with $K_d = \frac{\mathrm{k}}{6}$ proved to be effective to traverse over the obstacle in every five trials, where by average it took 22.6s for the whole robot to move over the obstacle.

Fig. 15 shows the experiment, where the robot successfully moves over a stair-type obstacle with the height of 55% of the diameter of snake robot modules, where the blue plate attached to the top of the obstacle is only for higher friction and to avoid slipping and has been consistent for every experiments. As seen in Fig. 15, the robot is actually touching the obstacle and moving over it, instead of trying to avoid collision. It should be mentioned that, in this experiment, unlike similar works[13],[19], which prior knowledge about the position and exact height of the obstacle and pressure sensor signal is required to move over an obstacle, the robot was not provided with any information about the position

or dimension of the obstacle or pressure sensor data, hence the adaptability is achieved only because of the compliancy of the joints.

The compliancy of the joints in this experiment plays the most important role to achieve adaptability. In this test, once the robot touches the obstacle, the motor torque signal, measured using the elastic element will be treated as a feedback signal, as shown in Fig. 13 to alter the commanded joint angles, this is also evident in the experiment shown in Fig. 14.b, where changing the joint stiffness resulted in adaptation of the joint trajectory. Hence, as the result of using this control strategy the robot joints behave like a virtual spring (in response to external forces), which its stiffness can be varied actively.

However, it should be mentioned that, in case the amplitude of the wave in (3) is too small compared to the height of the obstacle, visual feedback from the head module camera should be combined with the presented method to increase the amplitude of the wave if necessary. Moreover, although the joint compliancy is an effective strategy for climbing over the stair type obstacle, in real world applications, one can consider varying the joint stiffness to increase the stiffness of the joint on smooth terrain for higher forward speed and decrease the stiffness to achieve higher adaptability based on visual feedback or other environmental information.

Finally, to investigate if this control strategy is applicable to other scenarios, where the height, width and number of obstacles are different, another test environment constructed as shown in Fig. 16. In this experiment the robot was commanded to start moving based on pedal wave motion pattern (3) with the same gait parameters as the previous tests with $K_d = {}^{\mathrm{K}}/_{6}$ to climb over two obstacles placed on the path of the robot with the dimensions as shown in Fig. 16. As can be seen in Fig. 16 the robot successfully climbs over the obstacles with the same gait parameters and desired stiffness, which shows the effectiveness of the proposed control strategy.

As shown in Fig. 16, the robot, without changing the gait parameters, can successfully traverse over two obstacles with the specified dimensions. This experiment is relatively more complicated than the previous test because the robot can simultaneously be in contact with three surfaces with different height

(See Online Resource. 4). Without the stiffness control, the robot can easily roll over to one side when moving over these obstacles because of the lack of side stability due to narrow width of the robot links. This is not an issue with the pedal wave motion on a smooth surface, because the robot progress on a straight line and the centre of mass of the robot will be located inside the convex hull of the contact points. However, on uneven terrain, the proposed stiffness control strategy partially addresses this issue by decreasing the amplitude of the oscillation of the middle joints. As shown in Fig. 10 and Fig. 11, the middle joints of the robot, i.e. the joints closer to the centre of mass of the robot, will be subject to higher external torque, hence because of the stability of the proposed admittance controller the amplitude of oscillation of these joints will be smaller compared to the joints further away from the centre of mass. Hence the centre of mass of the robot remain closer to the ground compared to open-loop control strategy, which increases the side stability. It should be mentioned that another method to address this issue is to design the robot with 3D joints to add lateral motion to compensate the narrow width of the links.

5 Conclusion

In this paper, design and manufacture of modular snake robot with 3D printed joints and Polyurethane based SEAs presented. Using finite element analysis, the optimized design for the elastic element obtained and the final part manufactured with water jet cutter, hence unlike similar works, design and development of the proposed design robot does not involve complicated and costly manufacturing process. The elastic element modeled as a zero order torsional spring and eventually the resolution of the torque measurement mechanism obtained to be 0.01Nm, which satisfied the design constraints. Moreover, the efficacy of the torque measurement mechanism verified by comparing experimental results with the results of a simulated dynamical model of pedal wave motion, which proved the effectiveness of the proposed mechanism. To investigate the effectiveness of active stiffness control strategy, an admittance controller also designed and implemented, and its effect studied in single joint of the robot, which showed that by changing stiffness the trajectory of the joint can be changed in response to external forces. Finally, the proposed controller implemented on the robot, which enabled

it to successfully climb over an obstacle with the height of 55% of the diameter of snake robot modules, which was not possible with open loop controller. This showed that compliancy is indeed an effective strategy for generating adaptive pedal wave motion. The next avenue of the future work, could be extending the proposed controller to 3D snake robot gaits, such as sidewinding and incorporating visual feedback from the head camera into the controller to take into account the case, which the wave amplitude is too small compared to the height of the obstacle.

References

[1] Hirose S. *Biologically inspired robots: snake-like locomotors and manipulators.* Oxford University Press, NewYork, USA, 1993.

[2] Rollinson D, Choset H. Pipe network locomotion with a snake robot. *Journal of Field Robotics*, 2016, **33**, 322–336.

[3] Marvi H, Gong C, Gravish N. Sidewinding with minimal slip: snake and robot ascent of sandy slopes. *Science*, 2014, **346**, 224–9.

[4] Transeth A A, Leine R I, Glocker C. Snake robot obstacle-aided locomotion: modeling, simulations, and experiments. *IEEE Transactions on Robotics*, 2008, **24**, 88-104.

[5] Hutchinson H F. About snakes. *Nature*, 1879, **20**, 528–530.

[6] Mosauer W. On the locomotion of snakes. Science, *American Association for the Advancement of Science*, 1932, **76**, 583–585.

[7] Gray J. The mechanism of locomotion in snakes. *The Journal of experimental biology*, 1946, **23**, 101-120.

[8] Toyoshima S, Tanaka M, Matsuno F. A study on sinus-lifting motion of a snake robot with sequential optimization of a hybrid system. *IEEE Transactions on Automation Science and Engineering*, 2014, **11**, 139–144.

[9] Hopkins J K K, Spranklin B W W, Gupta S K K. A survey of snake-inspired robot designs. *Bioinspiration & Biomimetics*, 2009, **4**, 21001.

[10] Liljebäck P, Pettersen K Y, Stavdahl O. Hybrid modelling and control of obstacle-aided Snake robot locomotion. *IEEE Transactions on Robotics*, 2010, **26**, 781-799.

[11] Ryu J-K, Chong N Y, You B J. Locomotion of snake-like robots using adaptive neural oscillators. *Intelligent Service Robotics*, 2009, **3**, 1–10.

[12] Li G, Zhang H, Zhang. Development of adaptive locomotion of a caterpillar-like robot based on a sensory feedback CPG model. *Advanced Robotics*, 2014, **28**, 389–401.

[13] Yamada H, Hirose S. Steering of pedal wave of a snake-like robot by superposition of curvatures. *Proceedings of 2010 IEEE/RSJ International Conference on Intelligent Robots and Systems*, Taipei, Taiwan, 2010, 419–424.

[14] Kano T, Watanabe Y, Satake F. Decentralized-controlled multi-terrain robot inspired by flatworm locomotion. *Advanced Robotics*, 2014, **28**, 523–531.

[15] Torricelli D, Gonzalez J, Weckx M. Human-like compliant locomotion: state of the art of robotic implementations. *Bioinspiration & Biomimetics*, 2016, **11**, 051002.

[16] Vespignani M, Melo K, Bonardi S. Role of compliance on the locomotion of a reconfigurable modular snake robot. *Proceedings of 2015 IEEE/RSJ International Conference on Intelligent Robots and Systems*, Hamburg, Germany, 2015, 2238–2245.
[17] Kandhari A, Huang Y, Daltorio K A. Body stiffness in orthogonal directions oppositely affects worm-like robot turning and straight-line locomotion. *Bioinspiration & Biomimetics*, 2018, **13**, 026003.
[18] Whitman, J, Ruscelli F, Travers M, Choset H. "Shape-based compliant control with variable coordination centralization on a snake robot. *Proceedings* of *2016 IEEE Conference on Decision and Control*, Las Vegas, USA, 2016, 5165-5170.
[19] Sato T, Kano T, Ishiguro A. A decentralized control scheme for an effective coordination of phasic and tonic control in a snake-like robot. *Bioinspiration & Biomimetics*, 2012, **7**, 016005.
[20] Liljebäck P, Pettersen K Y, Stavdahl O. *Snake robots: modelling, mechatronics, and control*. Springer Science & Business Media, 2012.
[21] Liljebäck P, Stavdahl Ø, Pettersen K Y. A modular and waterproof snake robot joint mechanism with a novel force/torque sensor. *Proceedings of 2012 IEEE International Conference on Intelligent Robots and Systems*, Vilamoura, Portugal, 2012, 4898–4905.
[22] Takaoka S, Yamada H, Hirose S. Snake-like active wheel robot ACM-R4.1 with joint torque sensor and limiter. *Proceedings of 2011* I*EEE International Conference on Intelligent Robots and Systems*, San Francisco, CA, USA, 2011,1081–1086.
[23] Rollinson D, Bilgen Y, Brown B. Design and architecture of a series elastic snake robot. *Proceedings of IEEE International Conference on Intelligent Robots and Systems*, Chicago, IL, USA, 2014, 4630-4636.
[24] Martins L T, Arend Tatsch C A, Maciel E H. A Polyurethane-based compliant element for upgrading conventional servos into series elastic actuators. *IFAC-PapersOnLine*, 2015, **48**, 112–117.
[25] Pratt G A, Williamson M . Series elastic actuators. *Proceedings of 1995 IEEE/RSJ International Conference on Intelligent Robots and Systems. Human Robot Interaction and Cooperative Robots*, Pittsburgh, PA, USA, 1995, 399–406.
[26] Zhao Y, Paine N, Jorgensen S . Impedance Control and Performance Measure of Series Elastic Actuators. *IEEE Transactions on Industrial Electronics*, 2018, **65**, 2817–2827.
[27] Kano T, Sato T, Kobayashi R. Local reflexive mechanisms essential for snakes' scaffold-based locomotion. *Bioinspiration & Biomimetics*, 2012, **7**, 46008.
[28] Tesch M, Lipkin K, Brown I. Parameterized and scripted gaits for modular snake robots. *Advanced Robotics*, 2009, **23**, 1131–1158.
[29] Chen L, Ma S, Wang Y. Design and modelling of a snake robot in traveling wave locomotion. *Mechanism and Machine Theory*, 2007, **42**, 1632–1642.
[30] Li G, Li W, Zhang J. Analysis and design of asymmetric oscillation for caterpillar-like locomotion. *Journal of Bionic Engineering*, 2015, **12,** 190–203.
[31] Moreira F, Abundis A, Aguirre M ,Castillo J, Bhounsule P, An inchworm-inspired robot based on modular body, Electronics and Passive Friction Pads Performing the Two-anchor Crawl Gait. *Journal of Bionic Engineering*, 2018, **15,** 820-826.
[32] Akbarzadeh A, Kalani H. Design and modeling of a snake robot based on worm-like locomotion. *Advanced Robotics*, 2012, **26**, 537–560.
[33] De Luca A, Book W. Robots with flexible elements, *Handbook of Robotics*. Springer, 2008, 287–319.
[34] Chen L, Ma S, Wang Y. Design and modelling of a snake robot in traveling wave locomotion. *Mechanism and Machine Theory*, 2007, **42,** 1632–1642.

[35] Kerdok A E, Biewener A A, Mcmahon T A. Energetics and mechanics of human running on surfaces of different stiffnesses. *Journal of Applied Physiology*, 2002, **92,** 469–478.
[36] Geyer H, Seyfarth A, Blickhan R. Compliant leg behaviour explains basic dynamics of walking and running. *Proceedings of the Royal Society B: Biological Sciences* 2006, 2861-2867.
[37] Hurst J W. *The role and implementation of compliance in legged locomotion*, PhD thesis, Carnegie Mellon University, Pittsburgh, USA, 2008.
[38] Calanca A, Muradore R, Fiorini P. Impedance control of series elastic actuators: Passivity and acceleration-based control. *Mechatronics*, 2017, **47**, 37–48.

Appendix

The details of matrix $M(\boldsymbol{q})$ in (4) is as follows:

$$M(\boldsymbol{q}) = m(\boldsymbol{\mathcal{B}}_1 + \boldsymbol{\mathcal{A}}\boldsymbol{\mathcal{S}}_{\boldsymbol{\theta}}\boldsymbol{\mathcal{C}})^T(\boldsymbol{\mathcal{B}}_1 + \boldsymbol{\mathcal{A}}\boldsymbol{\mathcal{S}}_{\boldsymbol{\theta}}\boldsymbol{\mathcal{C}}) + m(\boldsymbol{\mathcal{B}}_2 - \boldsymbol{\mathcal{A}}\boldsymbol{\mathcal{C}}_{\boldsymbol{\theta}}\boldsymbol{\mathcal{C}})^T(\boldsymbol{\mathcal{B}}_2 - \boldsymbol{\mathcal{A}}\boldsymbol{\mathcal{C}}_{\boldsymbol{\theta}}\boldsymbol{\mathcal{C}}) + J\boldsymbol{\mathcal{C}}^T\boldsymbol{\mathcal{C}}, \qquad \text{(A1)}$$

where m and j are the mass and moment of inertia of each link and other matrices are defined as follows:

$$\boldsymbol{V} = [1 \quad 1 \quad \dots \quad 1]^T_{N\times 1}$$

$$\boldsymbol{\mathcal{B}}_{1_{N\times(N+2)}} = [\boldsymbol{0}_{N\times N-1} \quad \boldsymbol{V} \quad \boldsymbol{0}_{N\times 1}]$$

$$\boldsymbol{\mathcal{B}}_{2_{N\times(N+2)}} = [\boldsymbol{0}_{N\times N-1} \quad \boldsymbol{0}_{N\times 1} \quad \boldsymbol{V}]$$

$$\boldsymbol{\mathcal{H}} = \begin{bmatrix} l & 0 & 0 & \dots & 0 \\ 2l & l & 0 & \dots & 0 \\ 2l & 2l & l & \dots & 0 \\ \vdots & \vdots & \vdots & \vdots & \vdots \\ 2l & 2l & 2l & \dots & l \end{bmatrix}_{N\times N},$$

$$\boldsymbol{A}_{N\times N} = -\boldsymbol{\mathcal{H}} + \frac{1}{N}\boldsymbol{V}\boldsymbol{V}^T\boldsymbol{\mathcal{H}},$$

$$\boldsymbol{\mathcal{F}} = \begin{bmatrix} 1 & 1 & 1 & \dots & 1 \\ 0 & 1 & 1 & \dots & 1 \\ 0 & 0 & 1 & \dots & 1 \\ \vdots & \vdots & \vdots & \vdots & \vdots \\ 0 & 0 & 0 & \dots & 0 \end{bmatrix}_{N\times N-1},$$

$$\boldsymbol{\mathcal{C}}_{N\times(N+2)} = [\boldsymbol{\mathcal{F}} \quad \boldsymbol{V} \quad \boldsymbol{0}_{N\times 2}],$$

$$\boldsymbol{\mathcal{S}}_{\boldsymbol{\theta}} = diag\big(sin(\theta_1), sin(\theta_2), \dots, sin(\theta_N)\big),$$
$$\boldsymbol{\mathcal{C}}_{\boldsymbol{\theta}} = diag\big(cos(\theta_1), cos(\theta_2), \dots, cos(\theta_N)\big).$$

The matrix $\boldsymbol{C}(\boldsymbol{q}, \dot{\boldsymbol{q}})$ in the model presented in (4) can be obtained as follows:

$$\boldsymbol{C}(\boldsymbol{q}, \dot{\boldsymbol{q}}) =$$

$$m\big\{\boldsymbol{B}_1^T\boldsymbol{A}\boldsymbol{\mathcal{C}}_{\boldsymbol{\theta}}\boldsymbol{diag}(\boldsymbol{\mathcal{C}}\dot{\boldsymbol{q}})\boldsymbol{\mathcal{C}} + \boldsymbol{\mathcal{C}}^T\boldsymbol{\mathcal{C}}_{\boldsymbol{\theta}}\boldsymbol{diag}(\boldsymbol{\mathcal{C}}\dot{\boldsymbol{q}})\boldsymbol{A}^T\boldsymbol{B}_1 + \boldsymbol{\mathcal{C}}^T\boldsymbol{\mathcal{S}}_{\boldsymbol{\theta}}\boldsymbol{A}^T\boldsymbol{A}\boldsymbol{\mathcal{C}}_{\boldsymbol{\theta}}\boldsymbol{diag}(\boldsymbol{\mathcal{C}}\dot{\boldsymbol{q}})\boldsymbol{\mathcal{C}} + \boldsymbol{\mathcal{C}}^T\boldsymbol{\mathcal{C}}_{\boldsymbol{\theta}}\boldsymbol{diag}(\boldsymbol{\mathcal{C}}\dot{\boldsymbol{q}})\boldsymbol{A}^T\boldsymbol{A}\boldsymbol{\mathcal{S}}_{\boldsymbol{\theta}}\boldsymbol{\mathcal{C}}\big\}\dot{\boldsymbol{q}}$$

$$+m\{\boldsymbol{B_2^T A S_\theta diag(C\dot{q})C + C^T S_\theta diag(C\dot{q})A^T B_2 - C^T C_\theta A^T A S_\theta diag(C\dot{q})C} \\ \boldsymbol{- C^T S_\theta diag(C\dot{q})A^T A C_\theta C}\}\dot{\boldsymbol{q}}$$

$$+\frac{m}{2}\begin{bmatrix} \dot{\boldsymbol{q}}^T \boldsymbol{B_1}^T \boldsymbol{A C_\theta diag(C_1)C\dot{q}} \\ \dot{\boldsymbol{q}}^T \boldsymbol{B_1}^T \boldsymbol{A C_\theta diag(C_2)C\dot{q}} \\ \vdots \\ \dot{\boldsymbol{q}}^T \boldsymbol{B_1}^T \boldsymbol{A C_\theta diag(C_{2N+1})C\dot{q}} \end{bmatrix} + \frac{m}{2}\begin{bmatrix} \dot{\boldsymbol{q}}^T \boldsymbol{C^T C_\theta diag(C_1)A^T B_1\dot{q}} \\ \dot{\boldsymbol{q}}^T \boldsymbol{C^T C_\theta diag(C_2)A^T B_1\dot{q}} \\ \vdots \\ \dot{\boldsymbol{q}}^T \boldsymbol{C^T C_\theta diag(C_{2N+1})A^T B_1\dot{q}} \end{bmatrix}$$

$$+\frac{m}{2}\begin{bmatrix} \dot{\boldsymbol{q}}^T \boldsymbol{B_2}^T \boldsymbol{A S_\theta diag(C_1)C\dot{q}} \\ \dot{\boldsymbol{q}}^T \boldsymbol{B_2}^T \boldsymbol{A S_\theta diag(C_2)C\dot{q}} \\ \vdots \\ \dot{\boldsymbol{q}}^T \boldsymbol{B_2}^T \boldsymbol{A S_\theta diag(C_{2N+1})C\dot{q}} \end{bmatrix} + \frac{m}{2}\begin{bmatrix} \dot{\boldsymbol{q}}^T \boldsymbol{C^T S_\theta diag(C_1)A^T B_2\dot{q}} \\ \dot{\boldsymbol{q}}^T \boldsymbol{C^T S_\theta diag(C_2)A^T B_2\dot{q}} \\ \vdots \\ \dot{\boldsymbol{q}}^T \boldsymbol{C^T S_\theta diag(C_{2N+1})A^T B_2\dot{q}} \end{bmatrix}$$

$$+\frac{m}{2}\begin{bmatrix} \dot{\boldsymbol{q}}^T \boldsymbol{(C^T C_\theta diag(C_1)A^T MAS_\theta C + C^T S_\theta A^T MAC_\theta diag(C_1)C)\dot{q}} \\ \dot{\boldsymbol{q}}^T \boldsymbol{(C^T C_\theta diag(C_2)A^T AS_\theta C + C^T S_\theta A^T AC_\theta diag(C_2)C)\dot{q}} \\ \vdots \\ \dot{\boldsymbol{q}}^T \boldsymbol{(C^T C_\theta diag(C_{2N+1})A^T AS_\theta C + C^T S_\theta A^T AC_\theta diag(C_{2N+1})C)\dot{q}} \end{bmatrix}$$

$$-\frac{m}{2}\begin{bmatrix} \dot{\boldsymbol{q}}^T \boldsymbol{(C^T S_\theta diag(C_1)A^T AC_\theta C + C^T C_\theta A^T AS_\theta diag(C_1)C)\dot{q}} \\ \boldsymbol{v(C^T S_\theta diag(C_2)A^T AC_\theta C + C^T C_\theta A^T AS_\theta diag(C_2)C)\dot{q}} \\ \vdots \\ \dot{\boldsymbol{q}}^T \boldsymbol{(C^T S_\theta diag(C_{2N+1})A^T AC_\theta C + C^T C_\theta A^T AS_\theta diag(C_{2N+1})C)\dot{q}} \end{bmatrix}, \qquad \text{(A2)}$$

where

$$\boldsymbol{C_{N\times(N+2)} = [\mathcal{F} \quad V \quad 0_{N\times 2}] = [C_1, C_2, \dots, C_{N+2}]}$$

and gravitational force vector $\boldsymbol{\mathcal{G}}$ can be obtained to be:

$$\boldsymbol{\mathcal{G} = mgV^T(B_2 - AC_\theta C)}, \qquad \text{(A3)}$$

where g is the gravity constant.

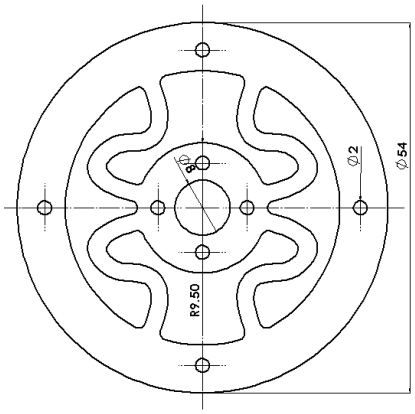

(a) CAD Model of the final elastic element design

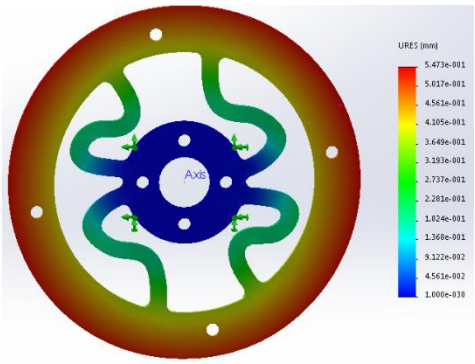

(b) Finite element analysis results

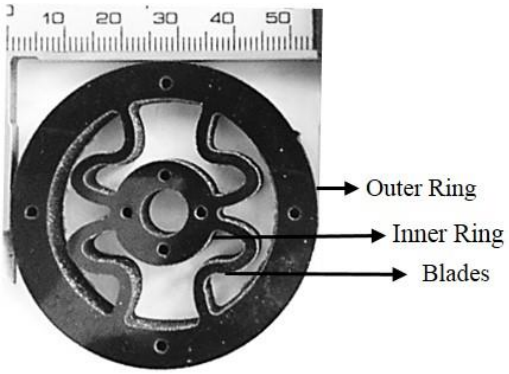

(c) The manufactured prototype with water-jet cutter

Fig. 1 The final design (dimensions are in millimeters).

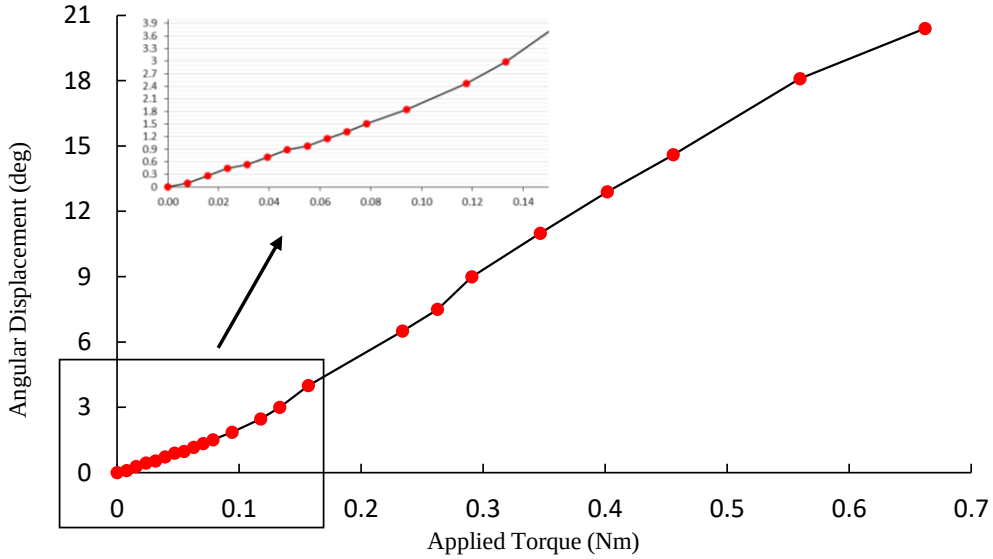

Fig. 2 Calibration results.

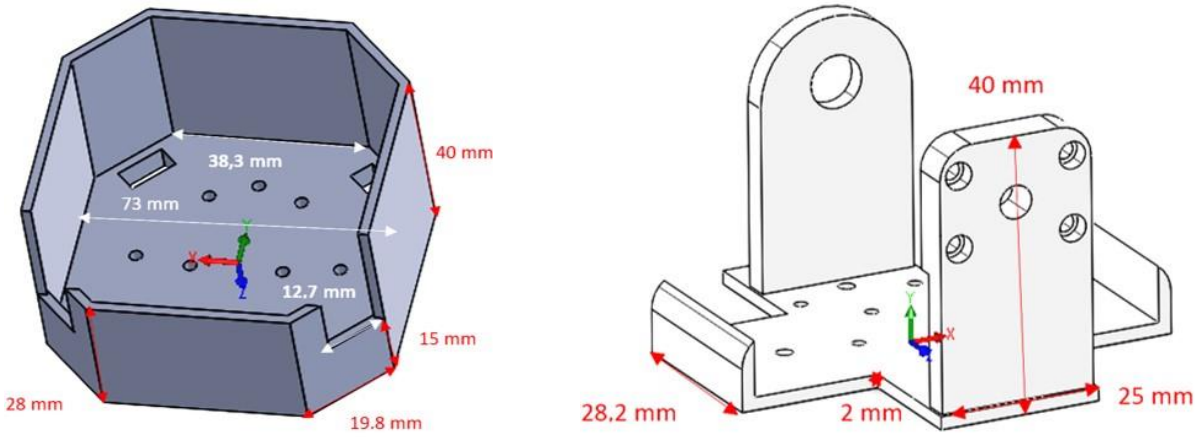

(a) Body design (b) Connector design

Fig. 3 Module main parts.

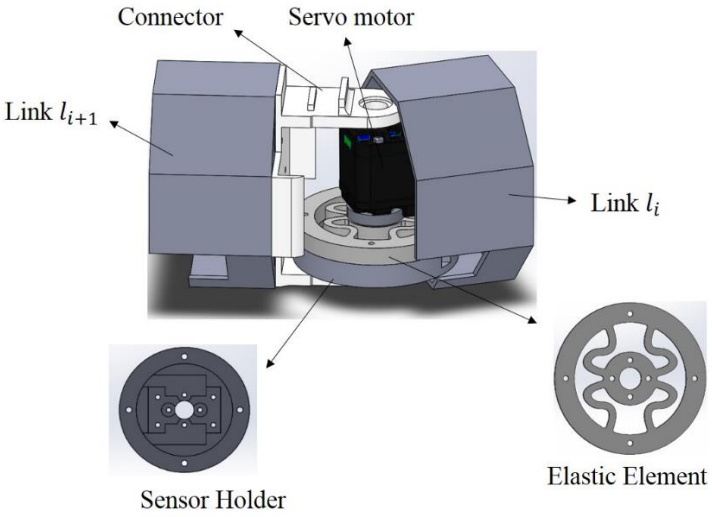

Fig. 4 CAD model of the assembled snake robot module.

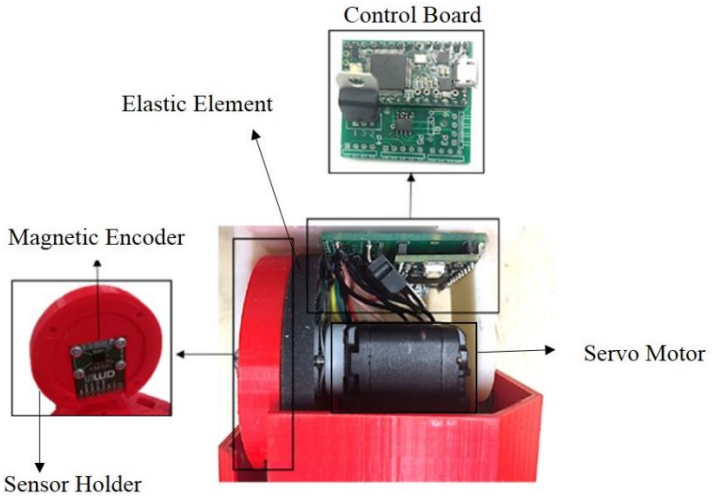

Fig. 5 Final joint assembly.

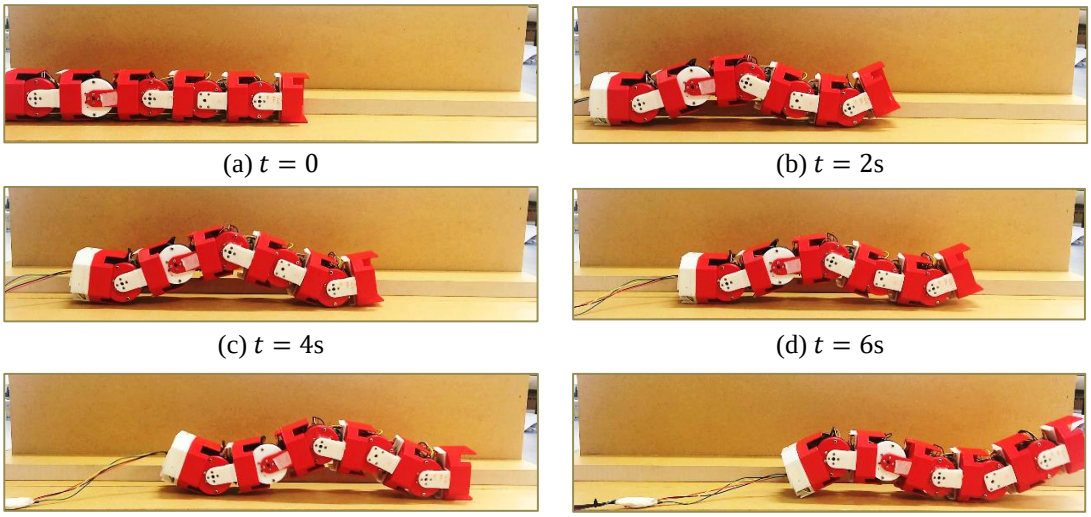

(a) $t = 0$ (b) $t = 2$s

(c) $t = 4$s (d) $t = 6$s

(e) $t = 8$s (f) $t = 10$s

Fig. 6 Snake progression with pedal wave motion.

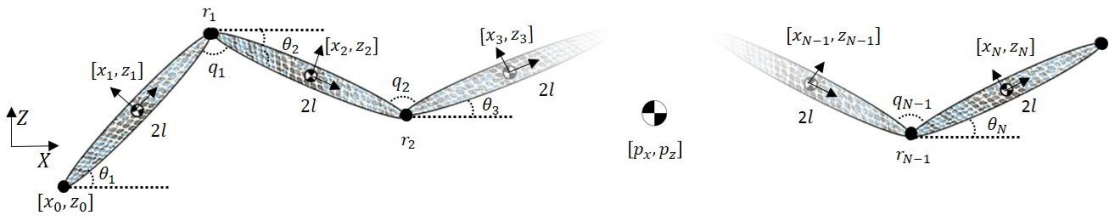

Fig. 7 Body shape of the robot performing pedal wave motion.

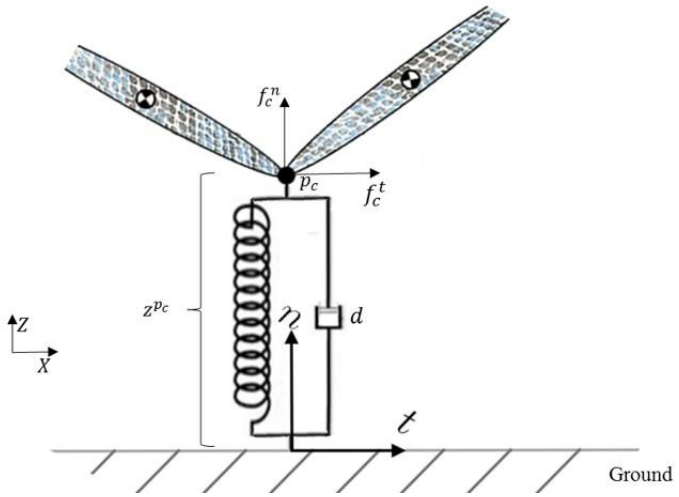

Fig. 8 Spring damper contact model.

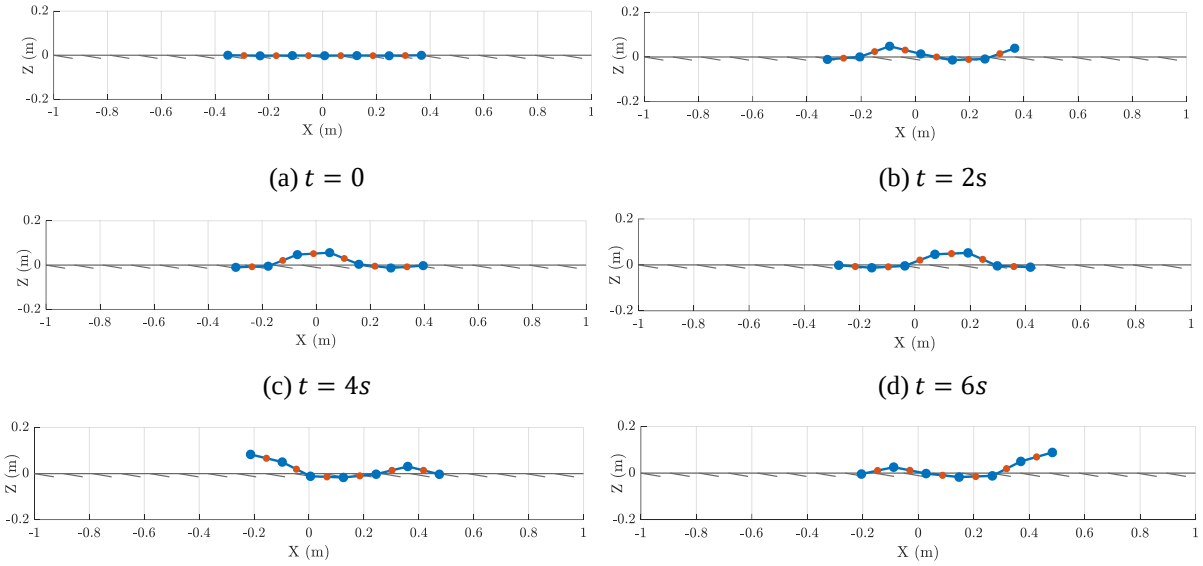

(a) $t = 0$ (b) $t = 2s$

(c) $t = 4s$ (d) $t = 6s$

(e) $t = 8s$ (f) $t = 10s$

Fig. 9 Simulated dynamical model of pedal wave motion.

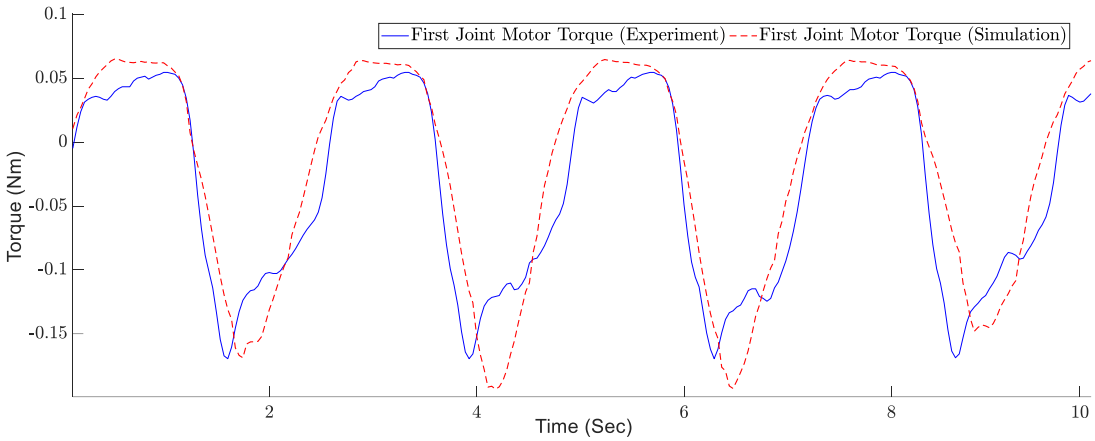

Fig. 10 First joint torque signal.

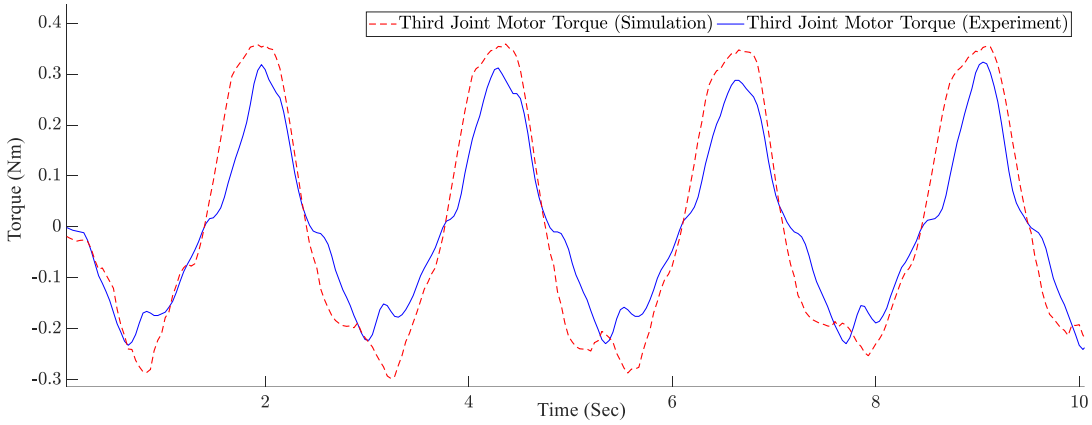

Fig. 11 Third joint torque signal.

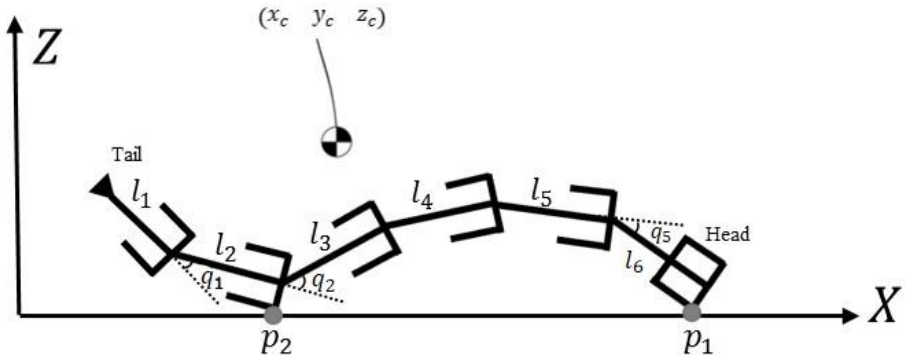

Fig. 12 The body shape of the snake robot during pedal wave motion.

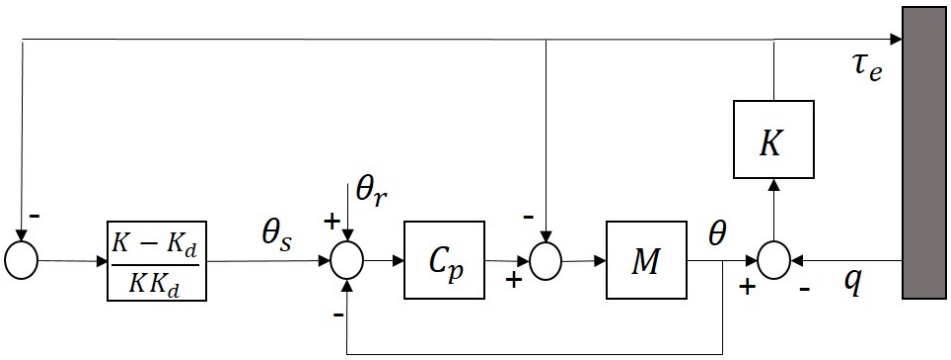

Fig. 13 Single joint admittance control block diagram.

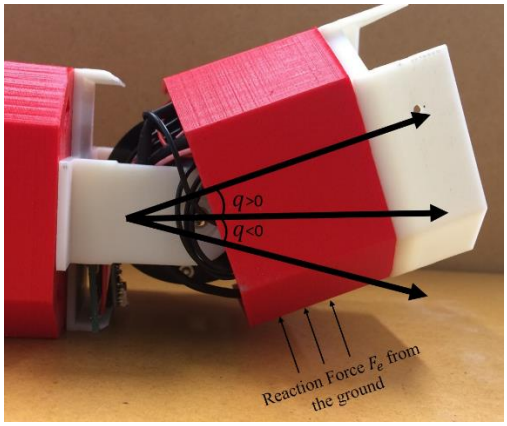

(a)

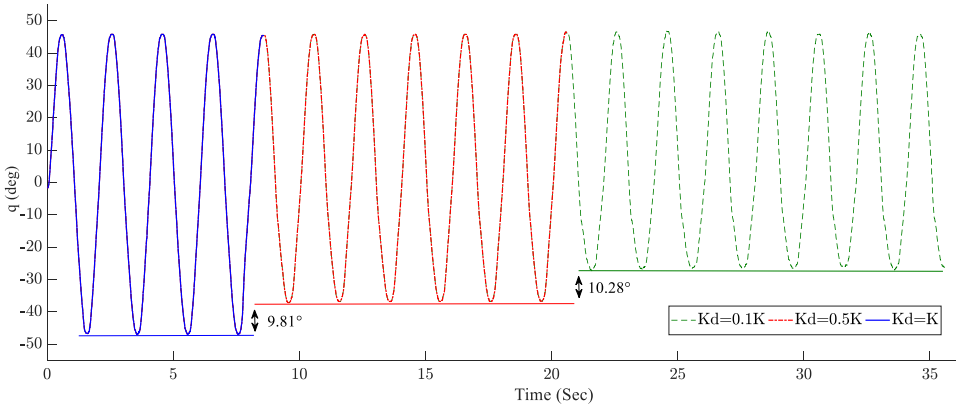

(b)

Fig. 14 The effect of varying joint stiffness on motion of the joint (a) Experiment set-up (b) Effect of $\boldsymbol{K_d}$ on joint angle $\boldsymbol{q}$

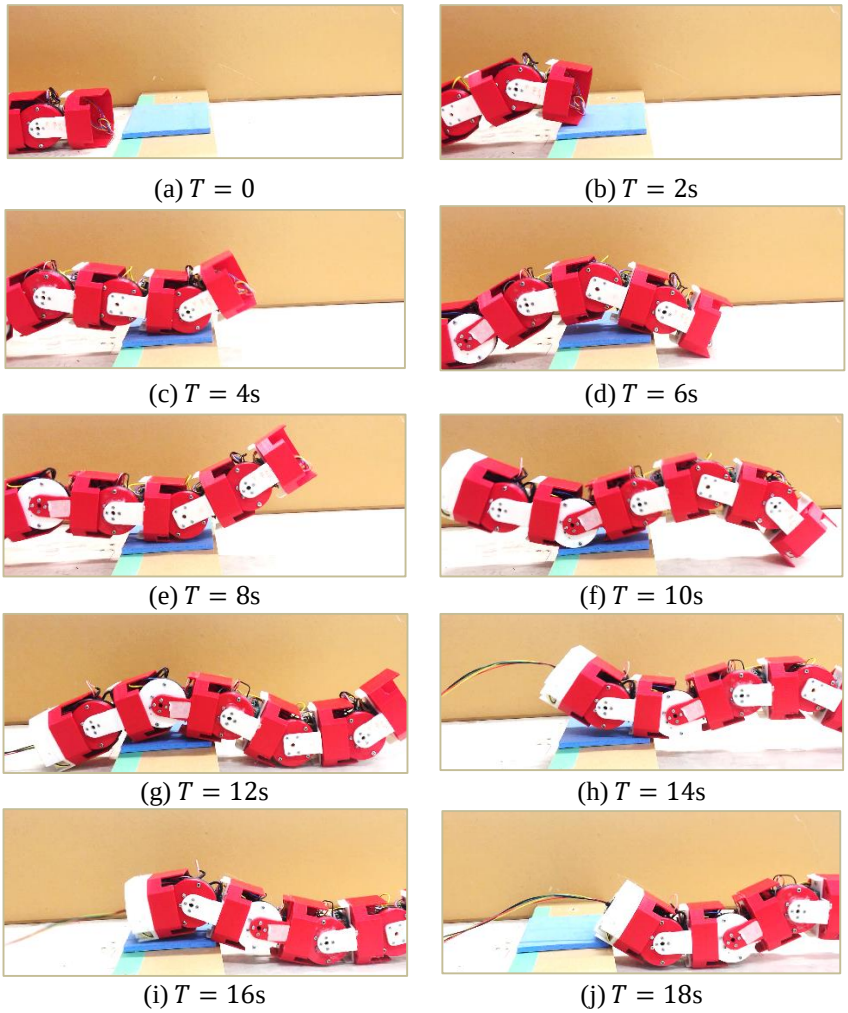

(a) $T = 0$ (b) $T = 2$s

(c) $T = 4$s (d) $T = 6$s

(e) $T = 8$s (f) $T = 10$s

(g) $T = 12$s (h) $T = 14$s

(i) $T = 16$s (j) $T = 18$s

Fig. 15 The robot climbing over an obstacle

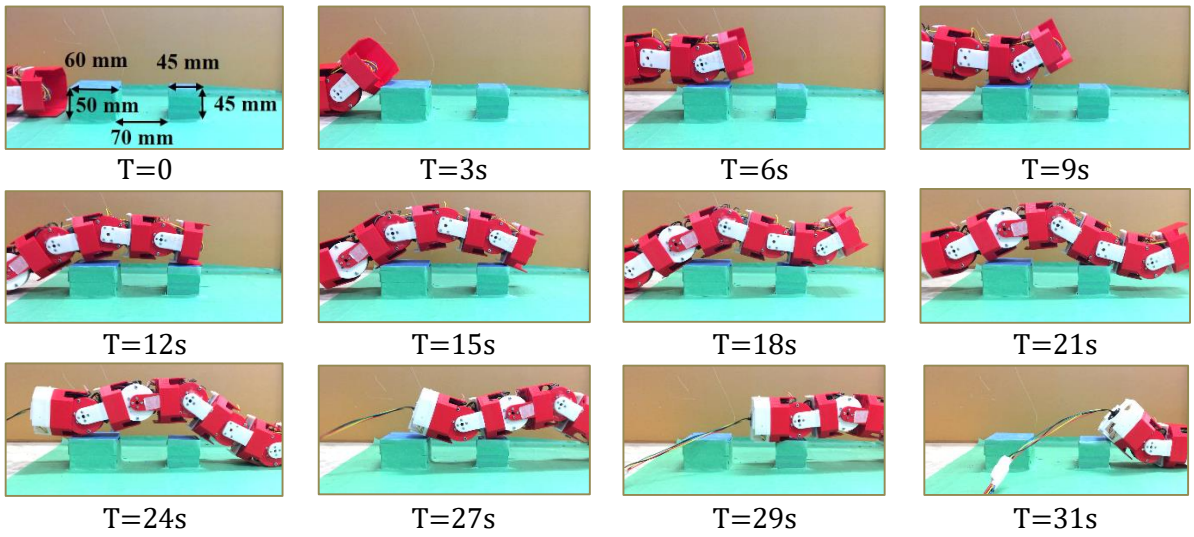

Fig. 16 The robot climbing over two obstacles

Table 1 Specifications of the servo motor

Dimensions (mm)	45(W)×24(D)×31(H)
Weight (g)	45
Nominal input voltage	7.4
Stall torque (kg.cm)	12
Maximum speed	6.30
Rotation angle range	5.58
Gear ratio	1:256

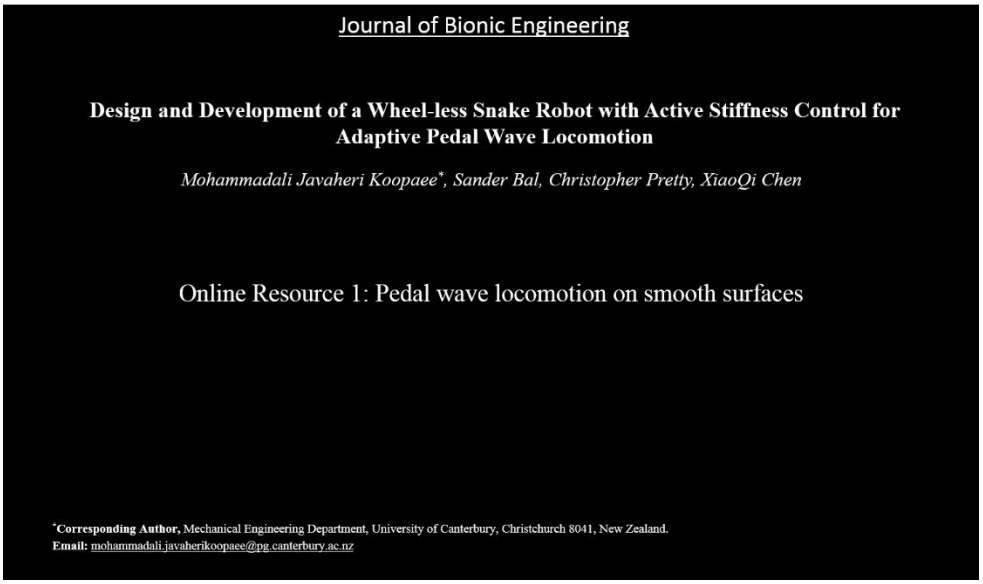

Online Resource. 1 The video demonstrating the pedal wave locomotion on smooth surfaces

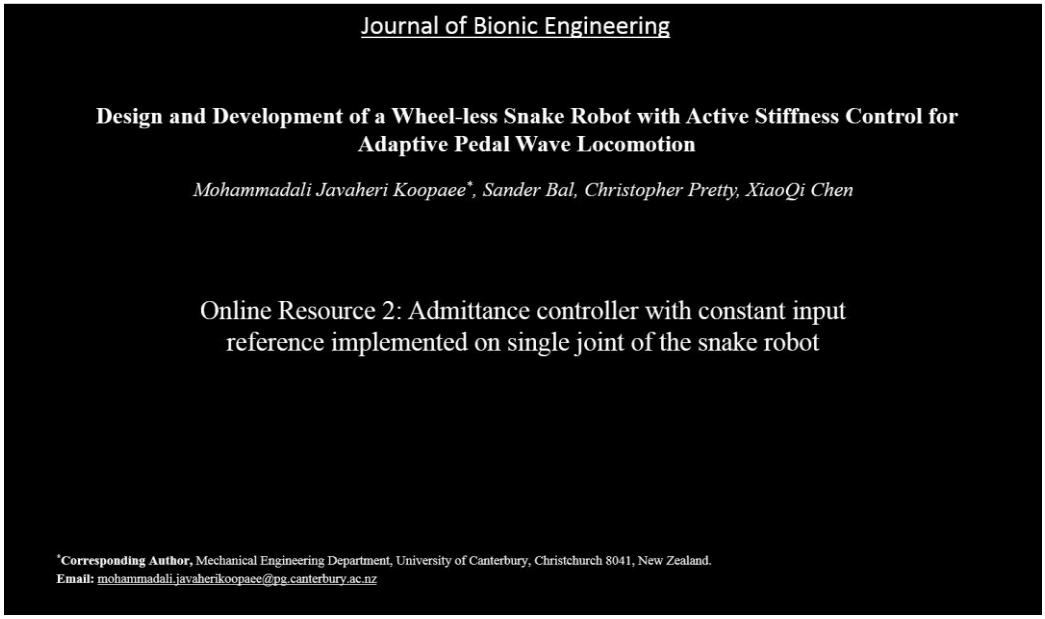

Online Resource. 2 The video showing the effect of admittance controller on single joint of the robot with constant input position reference

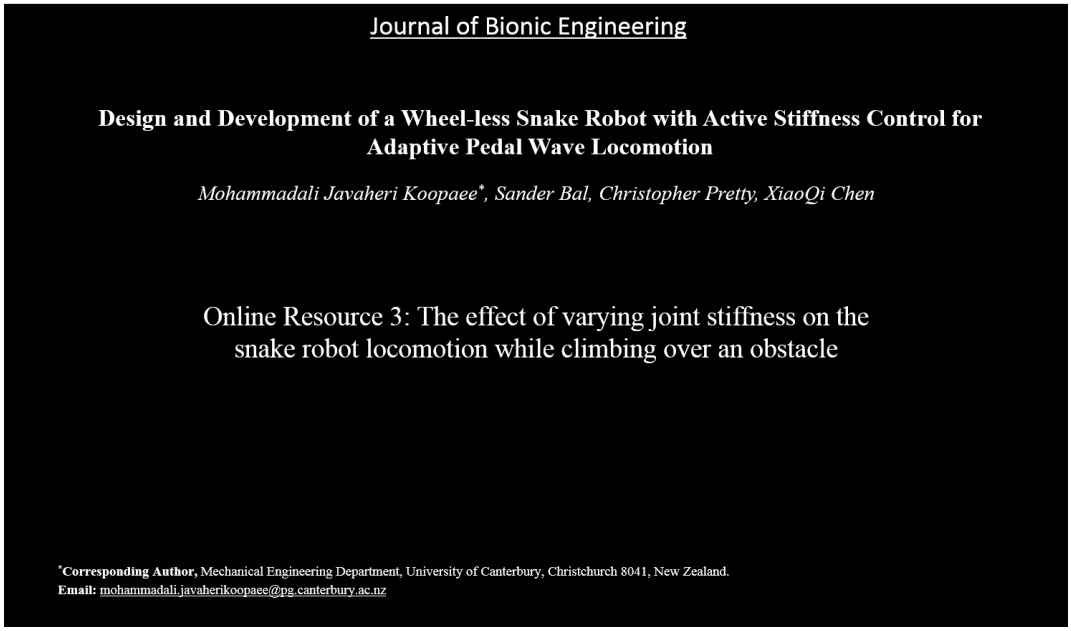

Online Resource. 3 The video demonstrating the effect of varying joint stiffness on the snake robot locomotion while climbing over an obstacle

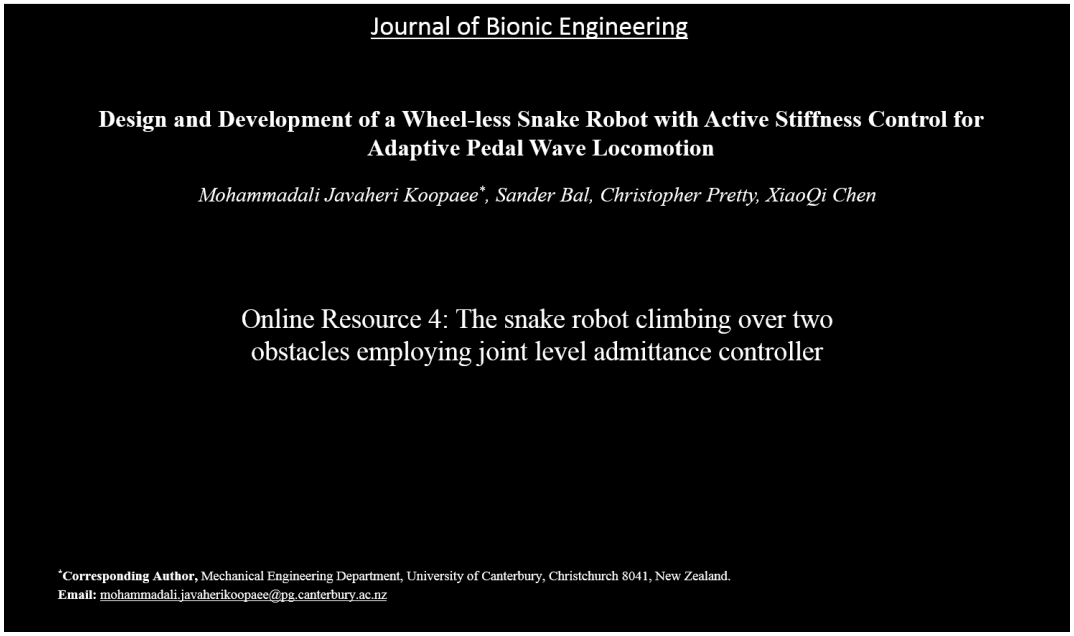

Online Resource. 4 The snake robot climbing over two obstacles employing joint level admittance controller

Table of figures

Fig. 1 The final design (dimensions are in millimeters).

Fig. 2 Calibration results.

Fig. 3 Module main parts.

Fig. 4 CAD model of the assembled snake robot module.

Fig. 5 Final joint assembly.

Fig. 6 Snake progression with pedal wave motion.

Fig. 7 Body shape of the robot performing pedal wave motion.

Fig. 8 Spring damper contact model.

Fig. 9 Simulated dynamical model of pedal wave motion.

Fig. 10 First joint torque signal.

Fig. 11 Third joint torque signal.

Fig. 12 The body shape of the snake robot during pedal wave motion.

Fig. 13 Single joint admittance control block diagram.

Fig. 14 The effect of varying joint stiffness on motion of the joint (a) Experiment set-up (b) Effect of Kd on joint angle q

Fig. 15 The robot climbing over an obstacle

Fig. 16 The robot climbing over two obstacles